PCCP

ROYAL SOCIETY OF CHEMISTRY

PAPER

View Article Online
View Journal | View Issue



Cite this: *Phys. Chem. Chem. Phys.*, 2024, **26**, 8419

# $[Ag(Sn_9–Sn_9)]^{5-}$ and $[(\eta^4\text{-}Sn_9)Ag(\eta^1\text{-}Sn_9)]^{7-}$, as aggregates of spherical aromatic building blocks. Persistence of aromaticity upon cluster gathering†

Peter L. Rodríguez-Kessler[a] and Alvaro Muñoz-Castro *[b]

Received 7th November 2023,
Accepted 19th February 2024

DOI: 10.1039/d3cp05394f

rsc.li/pccp

Formation of cluster-based materials requires a fundamental understanding of the resulting cluster aggregation processes. The $Sn_9^{4-}$ Zintl-ion structure can be viewed as a building block featuring a spherical aromatic species, leading to a cluster gathering upon oxidative coupling and/or mediated by transition metals. Here, we evaluate the spherical aromatic properties of $[Sn_9–Sn_9]^{6-}$, $[Ag(Sn_9–Sn_9)]^{5-}$ and $[(\eta^4\text{-}Sn_9)Ag(\eta^1\text{-}Sn_9)]^{7-}$, as aggregates of two $Sn_9$ building units held together *via* oxidative coupling and mediated by a Ag(I) transition metal center. Our results from magnetic criteria of aromaticity show that the inherent spherical aromatic characteristics of the parent $Sn_9^{4-}$ cluster are persistent in the overall aggregate where the enabled shielding cones ascribed to each $Sn_9$ unit are able to interplay between them, leading to an overlap of the shielding regions. Hence, the two approaches for bringing cluster units together are able to retain the inherent spherical aromatic features for each $Sn_9$ unit, leading to a cluster-based dimer where the parent properties remain. Thus, further cluster-based materials can be envisaged from aggregation upon oxidative coupling and/or mediated by transition metals, where the constituent building blocks retain their initial features, useful to guide the formation of more complex cluster-based aggregates.



## Introduction

Nine-atom deltahedral Zintl ions of group 14 have experienced a renewed interest in their chemistry during the past decade[1–7] owing to their unusual reactivity paving the way to further functionalizations reaching the formation of novel compounds. Coordination to transition metals, leads to the characterization of both *endo*- and *exo*-hedral intermetalloid clusters,[8] extending the rich structural diversity of Zintl ions displaying diverse electronic and bonding patterns.[9–17]

Several concepts have been applied to rationalize such species since the application of Lipscomb[18,19] pioneering contributions initially devoted to boron clusters,[20–23] underlying a correlation between structure and particular electron counts favoring special stability. The unique dependence on size unravels discontinuous property evolution, with particular behavior on a certain number of atoms and electrons capable of offering well-defined structures, desired for basic building block units, or superatoms,[24–27] on the making of nanoscale materials with defined properties. Their three-dimensional cages have been recognized to display spherical aromaticity[28,29] similar to *closo*-$[B_{12}H_{12}]^{2-}$,[19,21,30–33] favoring a unified view on their understanding despite of the different shapes and atom-types involved,[34,35] given their stabilizing electron delocalization from multicentre bonds.[36–40]

The controlled aggregation of Zintl-ions envisages further construction of molecular materials based on superatoms,[6,25] where finite and infinite chains have been obtained *via* oxidative coupling.[41–44] Moreover, *exo*-hedral transition metals serve to coordinate to different Zintl-ions,[11,45–50] resulting in another approach in connecting several cluster units in a single molecular structure.

Both planar and spherical aromatic species feature a characteristic behavior under an external magnetic field given by induced currents,[51,52] enabling a shielding induced magnetic field at the center with a complementary deshielding region at the outer contour.[53–58] Such effect is rationalized by the textbook shielding cone concept accounting for the nuclear shielding of neighbor atoms or molecules followed *via* NMR experiments,[59–63] and strongly related to aromatic species.

The characterization of $[Ag(Sn_9–Sn_9)]^{5-}$ (**1**) by Fässler group[64] reveals an effective aggregation of two deltahedral $[Sn_9]^{4-}$ units *via* both oxidative coupling and mediated by a

[a] *Centro de Investigaciones en Óptica A.C., Loma del Bosque 115, Col. Lomas del Campestre, León, Guanajuato, 37150, Mexico. E-mail: plkessler@cio.mx*
[b] *Facultad de Ingeniería, Arquitectura y Diseño, Universidad San Sebastián, Bellavista 7, Santiago, 8420524, Chile. E-mail: alvaro.munozc@uss.cl*

† Electronic supplementary information (ESI) available. See DOI: https://doi.org/10.1039/d3cp05394f

transition metal approaches, allowing to explore if the individual behavior of each Zintl-ion cage remains after the formation of **1**. In addition, the related $[(\eta^4\text{-}Sn_9)Ag(\eta^1\text{-}Sn_9)]^{7-}$ (**2**) cluster has been reported,[65] denoting the role of the overall anionic charge into the aggregation mode between two $[Sn_9]^{4-}$ units, now mediated exclusively by the transition metal cation. In this report, we evaluated the aromatic properties of the resulting aggregate in order to further understand the role of cluster gathering in the properties of each constituent cluster unit, given by $Sn_9$ cages, retaining or quenching the inherent properties displayed from the parent building blocks.

## Computational details

Geometry optimizations were performed by using DFT methods employing the ADF code[66] with triple-$\zeta$ Slater basis set plus the double-polarization functions (STO-TZ2P) within the hybrid PBE0 functional.[67,68] Relativistic effects were accounted by the scalar ZORA Hamiltonian.[69,70] The Grimme's empirical dispersion correction with the Becke–Johnson damping functions, D3(BJ), was employed for all the calculations.[71,72] The polarizable continuum model was incorporated by considering a conductor-like screening model treatment *via* the COSMO module[73,74] with ethylenediamine as a solvent to account for polar solvents and counterions. Shielding tensor ($\sigma$)[75] were calculated within the GIAO formalism, independent from atomic nuclei positions obtaining an overall representation of the magnetic response at the TZ2P/PBE0-ZORA-Scalar level of theory, by placing several points of the molecular domain in a box of $48 \times 48 \times 48$ bohr$^3$. In order to account for the induced magnetic field ($B^{ind}$), the following relation was applied $B^{ind} = -\sigma B^{ext}$ for each point within the cube array. For shielding tensor ($\sigma$) calculations, all electron triple-$\zeta$ Slater basis sets plus the double-polarization functions (STO-TZ2P) were employed.

## Results and discussion

The structure of $[Ag(Sn_9\text{–}Sn_9)]^{5-}$ (**1**) (Fig. 1), involves a coupled $[Sn_9\text{–}Sn_9]^{6-}$ *cis*-core from two $[Sn_9]^{4-}$ units sharing an *exo*-Sn–Sn bond able to further coordinate a Ag(I) atom, leading to several $AgSn_2$ motifs. For the free $[Sn_9\text{–}Sn_9]^{6-}$ skeleton, the *trans*-conformation is favored by −5.9 kcal mol$^{-1}$ in comparison to the *cis*- counterpart, larger than previously calculated at the B3LYP level,[64] denoting that the Ag(I) coordination is required to achieve the observed arrangement. **1** involves two $Sn_9$ units that are ascribed as tricapped trigonal prismatic (ttp) cages (pseudo-$D_{3h}$ symmetry) as given by the comparison of internal angles, with values of $\phi = 0.04$.[76] The calculated Sn–Ag distances show distances of 2.901, 2.901, and 2.999 Å, which are in line with the characterized experimentally of 2.880, 2.929, and 3.010 Å,[64] denoting a the distortion provided by counterions and packing effect upon crystallization. Such distances exhibit a small deviation from an ideal $\eta^3$-hapticity of Ag(I) over a deltahedral $Sn_3$ face.

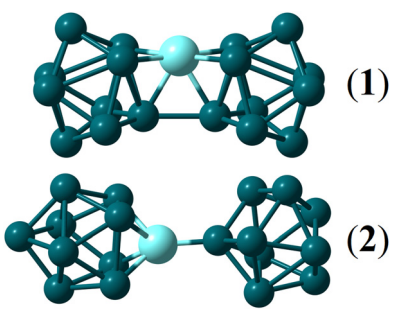


Fig. 1 Schematic representation of $[Ag(Sn_9\text{–}Sn_9)]^{5-}$ (**1**) and $[(\eta^4\text{-}Sn_9)Ag(\eta^1\text{-}Sn_9)]^{7-}$ (**2**) clusters.

Interestingly, a related $[(\eta^4\text{-}Sn_9)Ag(\eta^1\text{-}Sn_9)]^{7-}$ (**2**) cluster exhibits a different arrangement with the $Ag^+$ atom coordinated over a four-fold face of $Sn_9$ ($\eta^4$-) later connected to the next cage *via* a $\eta^1$-$Sn_9$ coordination,[65] given by the different anionic charge. The calculated Sn–Ag distances on the $Ag(\eta^4\text{-}Sn_9)$ side average 2.880 Å, whereas for $Ag(\eta^1\text{-}Sn_9)$ amounts to 2.703 Å, which compares well to experimental values of 2.889 and 2.713 Å, respectively. The two deltahedral units can be viewed as a monocapped square antiprism (msa) cage ($\sim C_{4v}$) with values of $\phi = 0.93$ for $\eta^4$-$Sn_9$, and $\eta^1$-$Sn_9$ as an $\sim C_{2v}$ intermediate. In overall, the calculated **1** and **2** structures exhibits a root mean square deviation (RMSD) of 0.126 and 0.128 Å, ascribed to structural variations upon crystallization which may decrease Sn–Sn bond distances which contributes to the observed calculated of RMSD.

Comparison between **1** and **2** structures at −5 and −7 charge states denotes that **1** is favored over **2** structure by 20.0 kcal mol$^{-1}$ at the −5 charge, whereas **2** is preferred over **1** structure by 3.0 kcal mol$^{-1}$ at −7 charge, in line with experimental structural characterization. Such observation denotes that the structures are strongly dependent on the selected charge state owing to the electronic requirements of $Sn_9$ units to reach a −4 charge in a less Sn–Sn connected structure. Thus, this suggests that a more or less connected structure can be selectively achieved by modifying the overall charge state *via* chemical or electrochemical approaches.

In addition, an alternative $[(^3\mu\text{-}Sn_9)Ag(^3\mu\text{-}Sn_9)]^{5-}$ isomer is evaluated, in line to the structure obtained for $[(^3\mu\text{-}Sn_9)\text{-}Cd(^3\mu\text{-}Sn_9)_2]^{6-}$.[11] Such isomer in both staggered and eclipsed conformations are located at 10.2 and 9.0 kcal mol$^{-1}$ above **1**. In the −7 charge state, $[(^3\mu\text{-}Sn_9)Ag(^3\mu\text{-}Sn_9)]^{7-}$ is located 11.5 and 12.0 kcal mol$^{-1}$ above the structure for **2**, supporting the experimentally characterized structures to be favored among alternative isomers, which are discussed in the following analyses.

The $Ag^+$–$(Sn_9\text{–}Sn_9)^{6-}$ interaction in **1** is evaluated *via* the interaction energy ($\Delta E_{int}$, Table 1), which amounts to −457.3 kcal mol$^{-1}$, denoting a favorable $Ag^+$ coordination to the tin cage. For **2**, the $Ag^+$–$[(\eta^4\text{-}Sn_9)(\eta^1\text{-}Sn_9)]^{8-}$ interaction exhibits a $\Delta E_{int}$ amounting to −539.6 kcal mol$^{-1}$, showing an increase in comparison to **1**. The $\Delta E_{int}$ quantity is further evaluated from the contribution from different chemically meaningful terms, according to the energy decomposition analysis (EDA) within the Ziegler–Rauk scheme,[77,78] according to:[77,79–82]

Table 1 Energy decomposition analysis (EDA) for the respective $Ag^+$–($Sn_9$–$Sn_9$) interaction in **1** and **2**. Values in kcal $mol^{-1}$

| | 1 | | 2 | |
|---|---|---|---|---|
| $\Delta E_{Pauli}$ | 157.2 | | 141.7 | |
| $\Delta E_{elstat}$ | −487.2 | 79.3% | −555.5 | 81.5% |
| $\Delta E_{orb}$ | −119.7 | 19.5% | −121.2 | 17.8% |
| $\Delta E_{disp}$ | −7.6 | 1.2% | −4.7 | 0.7% |
| $\Delta E_{int}$ | −457.3 | | −539.6 | |
| $\Delta\rho_1$ | −55.6 | 46.5% | −52.0 | 42.9% |
| $\Delta\rho_2$ | −16.0 | 13.4% | −17.4 | 14.4% |
| $\Delta\rho_3$ | −14.0 | 11.7% | −11.0 | 9.1% |
| $\Delta\rho_4$ | −9.4 | 7.9% | −11.0 | 9.1% |

$$\Delta E_{int} = \Delta E_{Pauli} + \Delta E_{elstat} + \Delta E_{orb} + \Delta E_{disp}$$

$\Delta E_{elstat}$ and $\Delta E_{orb}$ account for the stabilizing electrostatic and orbital character of the interaction, respectively, whereas $\Delta E_{Pauli}$ is related to the repulsive four-electron two-orbital interactions between occupied orbitals, giving rise to steric hindrance between interacting fragments.[83] Lastly, London dispersion interactions ($\Delta E_{disp}$) are taken into account *via* the pairwise correction of Grimme's[84] (DFT-D3BJ). Moreover, the basis set superposition error (BSSE) in the fragment interaction analysis to $\Delta E_{orb}$, was corrected *via* the counterpoise method.

The nature of the interaction ($\Delta E_{int}$) can be evaluated by the relative contributions from stabilizing terms, $\Delta E_{elstat}$, $\Delta E_{orb}$, and $\Delta E_{disp}$. For **1** and **2**, silver-tin cage interaction is of main electrostatic character, owing to the larger contribution from $\Delta E_{elstat}$, accounting for 79.3% and 81.5% of the electronic stabilizing terms, respectively. The orbital contribution ($\Delta E_{orb}$) accounts for 19.5% and 17.8%, of the stabilization with a small extent from London dispersion term (1.2% and 0.7%, respectively). In this sense, the bonding scheme contributing to the overall stabilization upon coordination of the silver atom is evaluated *via* the natural orbitals for chemical valence extension of the EDA method (EDA-NOCV), dissecting the $\Delta E_{orb}$ term into individual bonding contributions (Fig. 2).[80,85] A main cage → 5s-$Ag^+$ density deformation channels ($\Delta\rho_1$) is found to account for 46.5% and 42.9% of orbital contribution for **1** and **2**, respectively, which is later contributed by two cage → 5p-$Ag^+$ density deformation channels ($\Delta\rho_2$, $\Delta\rho_3$) with an overall contribution of 25.0% and 23.5%, respectively for each cluster. Lastly, a $\Delta\rho_4$ channel involves a cage ← 4d-$Ag^+$ backdonation contributing to 7.9% and 9.1% in **1** and **2**, respectively. In both clusters, the net charge at the silver center is similar to +0.43 ē, in line with previous calculations,[64] denoting the net charge transfer character of the Ag–$Sn_{18}$ coordination.

The two bridged spherical aromatic $Sn_9$ units in the formation of **1** and **2**, are able to retain similar structural features from the free $[Sn_9]^{4-}$ cluster, thus suggesting the plausible capabilities to embrace their inherent spherical aromatic characteristics. The calculated nucleus independent chemical shift (NICS),[86,87] employed to evaluate aromatic properties in both organic and inorganic species, denotes shielding values of −57.9 ppm at the center for the $Sn_9$ units and of −25.3 ppm

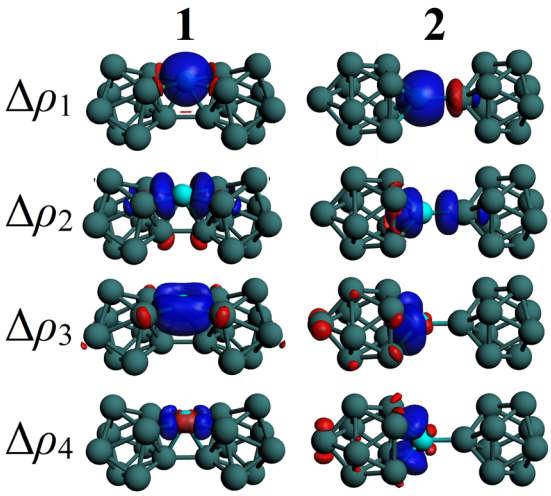


Fig. 2 Deformation density channels from EDA-NOCV analysis for the Ag–$Sn_{18}$ coordination. Charge flow from red to blue isosurfaces.

at the center of the $AgSn_6$ motif in **1**. For **2**, the values at the center of each $Sn_9$ unit is similar amounting to −55.1 ppm. Hence, the aggregated $Sn_9$ units in **1** and **2**, exhibit values in line to the calculated for bare $[Sn_9]^{4-}$ cluster of −57.8 ppm at the current level of theory, which is decreased in comparison to previous reports at the 6-311+G**/B3LYP(LANL2DZp) level (−68.2 ppm).[28] For $[Sn_9]^{2-}$, a decrease in the aromatic characteristics is given owing to the decrease of the NICS value at the center of the $Sn_9$ cage, which is calculated to amount to −38.9 ppm, similar to the previous reports at the 6-311+G**/B3LYP(LANL2DZp) level of (−38.3 ppm).[28] Such comparison between $[Sn_9]^{4-}$ and $[Sn_9]^{2-}$, expose that the decrease in number of electrons, decrease the shielding region inside the $Sn_9$ cage for the isolated cluster. However, upon oxidative coupling as in *cis*-/*trans*-$[Sn_9$–$Sn_9]^{6-}$ clusters, the central NICS values amounts to −56.1 and −51.2 ppm, respectively, denoting that the parent aromatic behavior of $[Sn_9]^{4-}$ is retained at the coupled aggregate, similarly to **1** and **2**.

In addition, an informative picture for $[Sn_9]^{4-}$ in terms of the adaptive natural density partitioning algorithm (AdNDP), have been provided in order to account for the aromatic properties according to the resulting bonding patterns as a set of multiple local σ-aromatic motifs.[88]

In order to account for the overall behavior of **1** and **2**, the isosurface representation of NICS values was obtained, which enables the study of the magnetic behaviour under different orientations, as an inherent characteristic of spherical aromatic structures. Shielding values denotes regions opposing the applied field (shielding or downfield shift), and deshielding values correspond to regions increasing the applied field (deshielding or upfield shift).[89] The NICS values account for the isotropic component dealing with the orientation-averaged response as a result of the experimental molecular tumbling in solution (Fig. 3).[90] For **1**, two spherical-like shielding regions are obtained following each $Sn_9$ unit, which is a common feature of spherical aromatic clusters, with the addition of a shielding region at the $AgSn_6$ section, supporting the spherical aromatic characteristics of the connected $Sn_9$ units and the

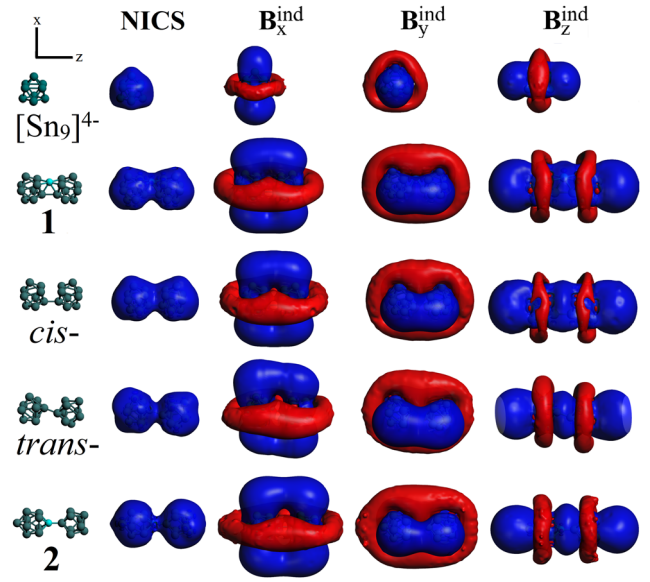


Fig. 3 Magnetic response properties for $[Sn_9]^{4-}$, **1** and **2**, and the related *cis*- and *trans*-$[Sn_9–Sn_9]^{6-}$ uncoordinated species, denoting the NICS (isotropic/averaged) term, and the behavior under specific orientations of the external field ($B_x^{ind}$, $B_y^{ind}$, and $B_z^{ind}$). Isosurfaces set to ±5 ppm, blue: shielding; red: deshielding.

central $AgSn_6$ motif. For the uncoordinated $[Sn_9–Sn_9]^{6-}$ skeleton at the *cis*- and *trans*-isomers, similar features are obtained, ascribed to each $Sn_9$ unit, denoting that the spherical-aromatic characteristics are retained in both coordinated and uncoordinated silver species. For comparison, the resulting NICS isosurface for the isolated $[Sn_9]^{4-}$ unit is provided, which features a related spherical-like shielding regions owing to its spherical aromatic characteristics,[28] which are retained in the overall structure for **1**.

Next, to unravel the aromatic characteristics in **1**, the formation of shielding cone characteristics[53,91–95] is evaluated by the shielding/deshielding response under particular orientations of the external magnetic field. For a field oriented along the *x*-axis ($B_x^{ind}$) two parallel shielding cones are unraveled, contained at each connected $Sn_9$ unit with a shielding region along the *x*-axis, and a complementary deshielding region perpendicular to the external field. Owing to the proximity of the $Sn_9$ units, both shielding and deshielding regions are overlapped. Along the *y*-axis ($B_x^{ind}$), a similar behavior is obtained, in line with the spherical aromatic characteristics which enable a shielding cone from any orientation of the external field, in contrast to planar aromatics where the shielding cone is reserved only for a perpendicularly oriented field in relation to the molecular plane.[96,97] For the isolated $[Sn_9]^{4-}$ unit, a similar behaviour is obtained, in line to its spherical aromatic characteristics denoting a shielding cone property from different orientations of the external field. Such difference between planar and spherical aromatics is given by the three-dimensional nature of the later as expected from the three-dimensional character of the electronic requirements, noted from the Hirsh $2(n + 1)^2$ rule, which fulfills consecutive spherical harmonic shells.[28]

Moreover, for a *z*-oriented field ($B_z^{ind}$), which is parallel to the $Sn_9–Sn_9$ axis, two parallel shielding cones are directly overlapped, similarly to the reported to the four-fold connected $[Sn_9–Sn_9–Sn_9–Sn_9]^{8-}$ ($Sn_{36}^{8-}$) cluster, as a 2.7 nm tin rod.[98] Thus, **1** and the related uncoordinated silver species are aggregates of adjacent spherical aromatic units retaining their inherent characteristics.

For **2**, the NICS isosurface exhibits similarly to **1**, two spherical-like shielding regions are obtained, which are allocated at both $Sn_9Ag$ and $Sn_9$ units. Despite the different structural arrangement in comparison to the more compact structure of **1**, two parallel shielding cones are enabled under an *x*- and *y*-axis oriented external field, denoting the spherical aromatic character of the two units within **2**. For a *z*-oriented field ($B_x^{ind}$), again, two parallel shielding cones are directly connected, revealing that despite the orientation of the external field, the shielding cone characteristics ascribed to each constituent unit are enabled, thus supporting that **2** is also an aggregate of spherical aromatic units. Hence, **1** and **2**, can be considered as two new examples of larger clusters composed of spherical-aromatic building blocks connected *via* Sn–Sn and Sn–Ag contacts, which retain their inherent spherical aromatic characteristics after aggregation, ascribed as two adjacent spherical aromatic states within a cluster.

From the cut plane representation (Fig. 4), the presence of two adjacent spherical aromatic units ascribed to each $Sn_9$ side is clearly denoted for **1**. The shielding region from the NICS isosurfaces overlaps, resulting in an extended shielding surface

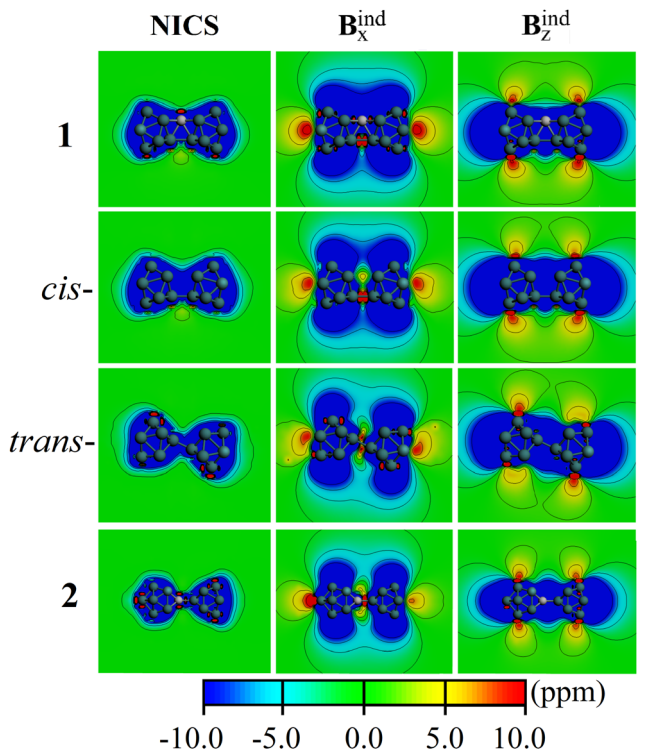


Fig. 4 Cut plane representation of the magnetic behavior for the studied species in order to complement Fig. 3.

ascribed to the overall backbone of the aggregated cluster. From a *z*-oriented external field, the resulting shielding cones overlap directly, increasing the extension of the shielding response. For the *x*-oriented field, the two parallel shielding cones overlap above and below the cluster structure, leaving a deshielding region in between the two aggregate $Sn_9$ units, as denoted in the uncoordinated $[Sn_9–Sn_9]^{6-}$ cluster in both *cis*- and *trans*-isomers (note that *trans*-isomer shows a lesser common shielding region of about $\sim -5.0$ ppm), which is overwhelm upon coordination of the Ag atom in **1**.

For **2**, similar features are found; however, as the two $Sn_9$ units are more separated than **1**, the continuous shielding surface from NICS overlaps at the Ag–Sn contact. For a *z*-oriented external field, the aligned shielding cones overlap directly, whereas, for an *x*-oriented field, the two parallel shielding cones share a $\sim -5.0$ ppm shielding region with a central deshielding region denoting that the two spherical aromatic units given by both ($\eta^4$-$Sn_9$)Ag and $Sn_9$ sides.

## Conclusions

The characterization of $[Ag(Sn_9–Sn_9)]^{5-}$ (**1**) and the related $[(\eta^4\text{-}Sn_9)Ag(\eta^1\text{-}Sn_9)]^{7-}$ (**2**) cluster, denotes two different fashion for cluster-cluster aggregation, involving oxidative coupling and mediated by Ag(I) coordination. Here, we explored the characteristics of each aggregated $Sn_9$ unit in such approaches in bringing together two cluster building blocks. The overall aromatic features of **1** and **2**, and related uncoordinated counterparts of **1**, are ascribed to the interplay between two spherical aromatic units, which retain the inherent spherical aromatic properties of the separated clusters. This result shows that different spherical aromatic circuits can be retained within a single and more complex molecular structure, representing the three-dimensional analog to the Clar's π-sextet rule. Thus, **1** and **2** are allowed to enable two different spherical aromatic circuits ascribed to each $Sn_9$ cluster building block, denoted as two spherical aromatic states.

Hence, such two cluster–cluster aggregation approaches, given by oxidative coupling and mediated by Ag(I) coordination, are able to retain the inherent characteristics of each building block upon cluster gathering. It is expected that the rational aggregation of well-defined building blocks will contribute to the formation of cluster-assembled materials, where each cluster unit retains the inherent cluster properties envisaging more extended examples.

## Conflicts of interest

There are no conflicts to declare.

## Acknowledgements

This work was supported by ANID FONDECYT Regular 1221676. P. L. R.-K (CVU 271425) would like to thank to Sistema Nacional de Investigadores (SNI) CONACYT for the financial support. Powered@NLHPC: This research was partially supported by the supercomputing infrastructure of the NLHPC (ECM-02).

## References

1 C. Liu and Z.-M. Sun, *Coord. Chem. Rev.*, 2019, **382**, 32–56.
2 S. Scharfe, F. Kraus, S. Stegmaier, A. Schier and T. F. Fässler, *Angew. Chem., Int. Ed.*, 2011, **50**, 3630–3670.
3 S. Fang, J. Li, K. Zou, H. Shuai, L. Xu, W. Deng, G. Zou, H. Hou and X. Ji, *Chem. Eng. J.*, 2022, **433**, 133841.
4 R. J. Wilson, B. Weinert and S. Dehnen, *Dalton Trans.*, 2018, **47**, 14861–14869.
5 S. C. Sevov and J. M. Goicoechea, *Organometallics*, 2006, 5678–5692.
6 S. M. Kauzlarich, *Chem. Mater.*, 2023, **35**, 7355–7362.
7 R. J. Wilson, N. Lichtenberger, B. Weinert and S. Dehnen, *Chem. Rev.*, 2019, **119**, 8506–8554.
8 T. F. Fässler and S. D. Hoffmann, *Angew. Chem., Int. Ed.*, 2004, **43**, 6242–6247.
9 W.-X. Chen, N. V. Tkachenko, A. Muñoz-Castro, A. I. Boldyrev and Z.-M. Sun, *Nano Res.*, 2022, **15**, 5705–5711.
10 J. Campbell, H. P. A. Mercier, H. Franke, D. P. Santry, D. A. Dixon and G. J. Schrobilgen, *Inorg. Chem.*, 2002, **41**, 86–107.
11 Y.-N. Yang, L. Qiao and Z.-M. Sun, *Chin. Chem. Lett.*, 2023, **34**, 107207.
12 B. Kesanli, J. Fettinger, D. R. Gardner and B. Eichhorn, *J. Am. Chem. Soc.*, 2002, **124**, 4779–4786.
13 M. M. Gillett-Kunnath, J. I. Paik, S. M. Jensen, J. D. Taylor and S. C. Sevov, *Inorg. Chem.*, 2011, **50**, 11695–11701.
14 C. Liu, L.-J. Li, X. Jin, J. E. McGrady and Z.-M. Sun, *Inorg. Chem.*, 2018, **57**, 3025–3034.
15 F. Li and S. C. Sevov, *Inorg. Chem.*, 2015, **54**, 8121–8125.
16 B. Kesanli, J. Fettinger and B. Eichhorn, *Chem. – Eur. J.*, 2001, **7**, 5277–5285.
17 A. Spiekermann, S. D. Hoffmann, F. Kraus and T. F. Fässler, *Angew. Chem., Int. Ed.*, 2007, **46**, 1638–1640.
18 W. N. Lipscomb, *Science*, 1977, **196**, 1047–1055.
19 R. B. King, B. Dai and B. M. Gimarc, *Inorg. Chim. Acta*, 1990, **167**, 213–222.
20 D. A. Dixon, D. A. Kleier, T. A. Halgren, J. H. Hall and W. N. Lipscomb, *J. Am. Chem. Soc.*, 1977, **99**, 6226–6237.
21 E. B. Moore, L. L. Lohr and W. N. Lipscomb, *J. Chem. Phys.*, 1961, **1329**, 1329–1334.
22 W. N. Lipscomb, A. R. Pitochelli and M. F. Hawthorne, *J. Am. Chem. Soc.*, 1959, **81**, 5833–5834.
23 W. N. Lipscomb, *J. Phys. Chem.*, 1957, **61**, 23–27.
24 A. W. Castleman and S. N. Khanna, *J. Phys. Chem. C*, 2009, **113**, 2664–2675.
25 E. A. Doud, A. Voevodin, T. J. Hochuli, A. M. Champsaur, C. Nuckolls and X. Roy, *Nat. Rev. Mater.*, 2020, **5**, 371–387.
26 M. F. Matus and H. Häkkinen, *Small*, 2021, **17**, 2170140.
27 M. F. Matus and H. Häkkinen, *Nat. Rev. Mater.*, 2023, **8**, 372–389.

28 A. Hirsch, Z. Chen and H. Jiao, *Angew. Chem., Int. Ed.*, 2001, **40**, 2834–2838.
29 R. B. King, *Chem. Rev.*, 2001, **101**, 1119–1152.
30 J. Poater, S. Escayola, A. Poater, F. Teixidor, H. Ottosson, C. Viñas and M. Solà, *J. Am. Chem. Soc.*, 2023, **145**, 22527–22538.
31 A. Muñoz-Castro, *Chem. Phys. Lett.*, 2013, **555**, 282–285.
32 J. Poater, C. Viñas, I. Bennour, S. Escayola, M. Solà and F. Teixidor, *J. Am. Chem. Soc.*, 2020, **142**, 9396–9407.
33 J. Poater, C. Viñas, M. Solà and F. Teixidor, *Nat. Commun.*, 2022, **13**, 3844.
34 C. Liu, I. A. Popov, Z. Chen, A. I. Boldyrev and Z.-M. Sun, *Chem. – Eur. J.*, 2018, **24**, 14583–14597.
35 N. V. Tkachenko, I. A. Popov, M. Kulichenko, N. Fedik, Z. Sun, A. Muñoz-Castro and A. I. Boldyrev, *Eur. J. Inorg. Chem.*, 2021, 4239–4250.
36 W.-M. Sun, Y. Li, D. Wu and Z.-R. Li, *J. Phys. Chem. C*, 2013, **117**, 24618–24624.
37 A. Y. Yu, *ChemistrySelect*, 2018, **3**, 4639–4642.
38 A. Tlahuice-Flores, A. Muñoz-Castro, A. Tlahuice-Flores and A. Muñoz-Castro, *Int. J. Quantum Chem.*, 2019, **119**, e25756.
39 X. Zhang, Y. Wang, H. Wang, A. Lim, G. Gantefoer, K. H. Bowen, J. U. Reveles and S. N. Khanna, *J. Am. Chem. Soc.*, 2013, **135**, 4856–4861.
40 A. Muñoz-Castro, *ChemPhysChem*, 2017, **18**, 87–92.
41 L. Xu and S. C. Sevov, *J. Am. Chem. Soc.*, 1999, **121**, 9245–9246.
42 R. Hauptmann and T. F. Fässler, *Z. Anorg. Allg. Chem.*, 2003, **629**, 2266–2273.
43 L. Yong, S. D. Hoffmann and T. F. Fässler, *Z. Anorg. Allg. Chem.*, 2005, **631**, 1149–1153.
44 A. Ugrinov and S. C. Sevov, *J. Am. Chem. Soc.*, 2002, **124**, 10990–10991.
45 A. Nienhaus, R. Hauptmann and T. F. Fässler, *Angew. Chem., Int. Ed.*, 2002, **41**, 3213–3215.
46 S. Scharfe and T. F. Fässler, *Eur. J. Inorg. Chem.*, 2010, 1207–1213.
47 B. Zhou, M. S. Denning, T. A. D. Chapman and J. M. Goicoechea, *Inorg. Chem.*, 2009, **48**, 2899–2907.
48 D. F. Hansen, B. Zhou and J. M. Goicoechea, *J. Organomet. Chem.*, 2012, **721–722**, 53–61.
49 C. Schenk, F. Henke, G. Santiso-Quiñones, I. Krossing and A. Schnepf, *Dalton Trans.*, 2008, 4436.
50 H. Xu, I. A. Popov, N. V. Tkachenko, Z. Wang, A. Muñoz-Castro, A. I. Boldyrev and Z. Sun, *Angew. Chem., Int. Ed.*, 2020, **59**, 17286–17290.
51 A. R. Eulenstein, Y. J. Franzke, N. Lichtenberger, R. J. Wilson, H. L. Deubner, F. Kraus, R. Clérac, F. Weigend and S. Dehnen, *Nat. Chem.*, 2021, **13**, 149–155.
52 I. Benkyi, H. Fliegl, R. R. Valiev and D. Sundholm, *Phys. Chem. Chem. Phys.*, 2016, **18**, 11932–11941.
53 R. Islas, T. Heine and G. Merino, *Acc. Chem. Res.*, 2012, **45**, 215–228.
54 G. Merino, T. Heine and G. Seifert, *Chem. – Eur. J.*, 2004, **10**, 4367–4371.
55 P. R. von Schleyer and H. Jiao, *Pure Appl. Chem.*, 1996, **68**, 209–218.
56 I. Fernandez, *Aromaticity*, Elsevier, Amsterdam, 2021.
57 B. J. Lampkin, P. B. Karadakov and B. VanVeller, *Angew. Chem., Int. Ed.*, 2020, **59**, 19275–19281.
58 P. B. Karadakov, *Org. Lett.*, 2020, **22**, 8676–8680.
59 J. A. Platts and K. Gkionis, *Phys. Chem. Chem. Phys.*, 2009, **11**, 10331.
60 A. S. Buchelnikov, G. I. Dovbeshko, D. P. Voronin, V. V. Trachevsky, V. V. Kostjukov and M. P. Evstigneev, *Appl. Spectrosc.*, 2014, **68**, 232–237.
61 R.-L. Lin, G.-S. Fang, W.-Q. Sun and J.-X. Liu, *Sci. Rep.*, 2016, **6**, 39057.
62 J. S. Mugridge, R. G. Bergman and K. N. Raymond, *J. Am. Chem. Soc.*, 2011, **133**, 11205–11212.
63 M. D. Peeks, T. D. W. Claridge and H. L. Anderson, *Nature*, 2016, **541**, 200–203.
64 J.-Q. Wang, B. Wahl and T. F. Fässler, *Angew. Chem., Int. Ed.*, 2010, **49**, 6592–6595.
65 F. S. Geitner, W. Klein and T. F. Fässler, *Dalton Trans.*, 2017, **46**, 5796–5800.
66 N.d.
67 C. Adamo and V. Barone, *J. Chem. Phys.*, 1999, **110**, 6158–6170.
68 M. Ernzerhof and G. E. Scuseria, *J. Chem. Phys.*, 1999, **110**, 5029.
69 E. van Lenthe, E.-J. J. Baerends and J. G. Snijders, *J. Chem. Phys.*, 1994, **101**, 9783.
70 E. van Lenthe, A. Ehlers and E.-J. Baerends, *J. Chem. Phys.*, 1999, **110**, 8943.
71 S. Grimme, J. Antony, S. Ehrlich and H. Krieg, *J. Chem. Phys.*, 2010, **132**, 154104.
72 S. Grimme, S. Ehrlich and L. Goerigk, *J. Comput. Chem.*, 2011, **32**, 1456–1465.
73 A. Klamt and V. Jonas, *J. Chem. Phys.*, 1996, **105**, 9972.
74 A. Klamt and G. Schüürmann, *J. Chem. Soc., Perkin Trans. 2*, 1993, 799–805.
75 G. Schreckenbach and T. Ziegler, *J. Phys. Chem.*, 1995, **99**, 606–611.
76 A. Muñoz-Castro and S. Sevov, *Phys. Chem. Chem. Phys.*, 2013, **15**, 986–991.
77 G. Te Velde, F. M. Bickelhaupt, E. J. Baerends, C. Fonseca Guerra, S. J. van Gisbergen, J. G. Snijders and T. Ziegler, *J. Comput. Chem.*, 2001, **22**, 931–967.
78 T. Ziegler and A. Rauk, *Theor. Chim. Acta*, 1977, **46**, 1–10.
79 M. von Hopffgarten and G. Frenking, *Wiley Interdiscip. Rev.: Comput. Mol. Sci.*, 2012, **2**, 43–62.
80 G. Frenking, M. Bickelhaupt and F. Matthias Bickelhaupt, in *Chem. Bond*, Wiley-VCH Verlag GmbH & Co. KGaA, Weinheim, Germany, 2014, pp. 121–157.
81 M. Solà, M. Duran and J. Poater, *Theor. Chem. Acc.*, 2021, **140**, 33.
82 D. M. Andrada and C. Foroutan-Nejad, *Phys. Chem. Chem. Phys.*, 2020, **22**, 22459–22464.
83 B. Pinter, T. Fievez, F. M. Bickelhaupt, P. Geerlings and F. De Proft, *Phys. Chem. Chem. Phys.*, 2012, **14**, 9846.
84 S. Grimme, *Wiley Interdiscip. Rev.: Comput. Mol. Sci.*, 2011, **1**, 211–228.
85 A. Michalak, R. L. DeKock and T. Ziegler, *J. Phys. Chem. A*, 2008, **112**, 7256–7263.

 

86 J. O. C. Jiménez-Halla, E. Matito, J. Robles and M. Solà, *J. Organomet. Chem.*, 2006, **691**, 4359–4366.
87 P. von, R. Schleyer, C. Maerker, A. Dransfeld, H. Jiao, N. J. R. van and E. Hommes, *J. Am. Chem. Soc.*, 1996, **118**, 6317–6318.
88 N. V. Tkachenko and A. I. Boldyrev, *Chem. Sci.*, 2019, **10**, 5761–5765.
89 M. Kaupp, M. Bühl and V. G. Malkin, *Calculation of NMR and EPR Parameters: Theory and Applications*, John Wiley & Sons, Inc., 2006.
90 J. C. C. Chan, *Solid State NMR*, Springer Berlin Heidelberg, Berlin, Heidelberg, 2012.
91 M. Buhl, M. Kaupp, V. G. Malkin and M. Bühl, *Calculation of NMR and EPR Parameters*, Wiley-VCH, Weinheim, FRG, 2004.
92 J. A. N. F. Gomes and R. B. Mallion, *Chem. Rev.*, 2001, **101**, 1349–1384.
93 D. Sitkoff and D. A. Case, *Prog. Nucl. Magn. Reson. Spectrosc.*, 1998, **32**, 165–190.
94 D. A. Case, *Curr. Opin. Struct. Biol.*, 1998, **8**, 624–630.
95 T. Heine, C. Corminboeuf and G. Seifert, *Chem. Rev.*, 2005, **105**, 3889–3910.
96 A. Muñoz-Castro, *Phys. Chem. Chem. Phys.*, 2017, **19**, 12633–12636.
97 A. G. Papadopoulos, N. D. Charistos and A. Muñoz-Castro, *ChemPhysChem*, 2017, **18**, 1499–1502.
98 N. V. Tkachenko, W.-X. Chen, H. W. T. Morgan, A. Muñoz-Castro, A. I. Boldyrev and Z.-M. Sun, *Chem. Commun.*, 2022, **58**, 6223–6226.